communications physics

ARTICLE

https://doi.org/10.1038/s42005-022-01021-y OPEN

Engineering non-Hermitian skin effect with band topology in ultracold gases

Lihong Zhou[1], Haowei Li[2,3], Wei Yi[2,3]✉ & Xiaoling Cui[1,4]✉

Non-Hermitian skin effect(NHSE) describes a unique non-Hermitian phenomenon that all eigen-modes are localized near the boundary, and has profound impact on a wide range of bulk properties. In particular, topological systems with NHSE have stimulated extensive research interests recently, given the fresh theoretical and experimental challenges therein. Here we propose a readily implementable scheme for achieving NHSE with band topology in ultracold gases. Specifically, the scheme realizes the one-dimensional optical Raman lattice with two types of spin-orbit coupling (SOC) and an additional laser-induced dissipation. By tuning the dissipation and the SOC strengths, NHSE and band topology can be individually controlled such that they can coexist in a considerable parameter regime. To identify the topological phase in the presence of NHSE, we have restored the bulk-boundary correspondence by invoking the non-Bloch band theory, and discussed the dynamic signals for detection. Our work serves as a guideline for engineering topological lattices with NHSE in the highly tunable environment of cold atoms, paving the way for future studies of exotic non-Hermitian physics in a genuine quantum many-body setting.

[1] Beijing National Laboratory for Condensed Matter Physics, Institute of Physics, Chinese Academy of Sciences, 100190 Beijing, China. [2] CAS Key Laboratory of Quantum Information, University of Science and Technology of China, 230026 Hefei, China. [3] CAS Center For Excellence in Quantum Information and Quantum Physics, 230026 Hefei, China. [4] Songshan Lake Materials Laboratory, 523808 Dongguan, Guangdong, China. ✉email: wyiz@ustc.edu.cn; xlcui@iphy.ac.cn

Open quantum systems undergoing particle or energy loss can be effectively described by non-Hermitian Hamiltonians. They exhibit intriguing non-Hermitian phenomena that are absent in their Hermitian counterparts and have thus attracted significant attention in recent years[1,2]. An outstanding example here is the non-Hermitian skin effect (NHSE)[3–20], under which all bulk eigenstates are localized near the boundary. While NHSE is topologically protected by the winding of eigen-spectrum in the complex energy plane[12,13], the spectrum itself is sensitive to the actual boundary condition. For instance, both the eigen-spectrum and eigen-wavefunction can be dramatically different under an open boundary condition (OBC) from those under a periodic boundary condition (PBC). A remarkable consequence is the failure of conventional bulk-boundary correspondence in topological systems with NHSE, whose restoration calls for the so-called non-Bloch band theory by employing a generalized Brillouin zone (GBZ)[3–6]. Apart from the fundamental impact on band topology, NHSE can strongly influence many other bulk properties such as the dynamics[9,16,21–23], the parity-time symmetry[24,25], and localization[26,27].

To date, NHSE has been observed in various non-Hermitian one-dimensional (1D) topological systems, including photonics[28–30], topoelectrical circuits[31], and metamaterials[32], wherein the non-Bloch bulk-boundary correspondence has also been confirmed[28,29,31]. In these studies, NHSE is predominantly achieved through non-reciprocal hopping, by simulating either the Hatano-Nelson model[33] or the nonreciprocal Su-Schrieffer-Heeger model[3]. At the moment, the study of NHSE deserves a substantial extension to a broader context. On the one hand, the appearance of NHSE is not limited to these models. For instance, a simple spin rotation in momentum space can directly convert the nonreciprocal hopping to on-site dissipation[3,34], under which NHSE persists[7,9,14–16]. On the other hand, given the existing experiments are either classical or on the level of single photons, it is desirable to engineer NHSE in a quantum many-body setting, which would offer exciting opportunities for investigating the interplay of NHSEs with many-body statistics and interactions.

Ultracold atomic gases, with highly controllable parameters, are an ideal candidate for the task. In this platform, through the photon-mediated Raman coupling technique, both the 1D and 2D spin-orbit couplings (SOC) have been realized[35–43], culminating in the successful generation of topological bands in optical lattices[42–46]. Meanwhile, laser-induced atom loss has enabled the experimental realization of parity-time symmetry in ultracold atoms[47–49], and a very recent experiment manages to incorporate the SOC with laser-induced loss in a single setup[49].

In light of these achievements, we propose to engineer NHSE with band topology in ultracold atoms by utilizing the Raman-assisted SOCs and laser-induced atom loss. Specifically, we consider a one-dimensional optical Raman lattice with two distinct types of SOCs, where the nontrivial band topology is facilitated by one type of SOC, and the NHSE originates from the other, along with the laser-induced loss. While both types of SOC are indispensable in inducing the NHSE with nontrivial band topology, they are not a trivial combination but exhibit a strong interplay effect in this process. We have mapped out the topological phase diagram, tabulated the parameter regimes for NHSE and band topology, and proposed the dynamical detection scheme. As all aspects of our proposal are readily accessible, our work represents a significant step toward the observation of NHSEs and the associated exotic phenomena in a genuine quantum many-body setting.

Results

Model. As illustrated in Fig. 1, we consider a two-component(↑,↓) atomic gas in a 1D optical lattice (along x), described by the Hamiltonian $H=\int dx H(x)$, with

$$H(x)=\frac{p_x^2}{2m}-V_0\cos(2k_0x)+M_0\sin k_0x(e^{i\phi_0}\sigma_+ + H.c.) + M_r(e^{i2k_rx}\sigma_+ + h.c.)+i\gamma\sigma_z. \quad (1)$$

Here $\sigma_\pm=\sigma_x\pm i\sigma_y$, with $\sigma_\alpha(\alpha=x,y,z)$ the Pauli matrices, and $\frac{p_x^2}{2m}$ is the kinetic term.

The optical Raman lattice[42,43,46], characterized by V_0 and M_0, is generated by two Raman lasers: a standing wave propagating along x with the electric-field vector $\mathbf{E}_{1x}=\mathbf{e}_z2E_{1x}e^{i\phi_{1+}}\cos(k_0x+\phi_{1-})$, where $\phi_{1\pm}=(\phi_{1x}\pm\phi'_{1x})/2$, and ϕ_{1x} (ϕ'_{1x}) is the phase of incident (reflected) light; and a plane wave propagating along z with $\mathbf{E}_{1z}=\mathbf{e}_xE_{1z}e^{ik_0z+\phi_{1z}}$. As shown in Fig. 1b, E_{1x} and E_{1z} come from the same laser source (laser 1) through a beam splitter, enabling easy manipulation of various relative phases. For instance, the phase $\phi_{1-}(=-k_0L_{1x})$ is adjustable through the optical-path L_{1x} from the sample (gray dot) to mirror M_1. By taking $\phi_{1-}=-\pi/2$ and $z=0$, the field $\mathbf{E}_{1x}$ generates a lattice potential with spacing $a=\pi/k_0$ and lattice sites at $x_i=ia$. $\mathbf{E}_{1x}$, $\mathbf{E}_{1z}$ combine to form the SOC that couples different spins with amplitude $M_0\sin(k_0x)$ and phase $\phi_0=\phi_{1+}-\phi_{1z}$. The phase $\phi_0=k_0(L_{1x}-2L_{1z})$ is tunable through L_{1x} or L_{1z}, with L_{1z} the perpendicular distance (along $\hat{z}$ between the mirrors M_2, M_3 and the sample).

An additional SOC, characterized by M_r and known as the equal Rashba and Dresselhaus coupling[35–39,44,45], is created by two plane-wave Raman lasers($\mathbf{E}_{2x}$,$\mathbf{E}'_{2x}$) with opposite wave-vectors along x and equal phase. As shown in Fig. 1b, $\mathbf{E}_{2x}$ and $\mathbf{E}'_{2x}$ are both from the laser source 2 (with wave-vector k_0) and intersect at the sample following reflections by two mirrors M_4, M_5. By adjusting the angle θ between their propagation directions and $\hat{x}$, the recoil momentum in (1) is tunable as $k_r=k_0\cos\theta$. Their relative phase can be tuned to zero, as is the case with (1), by adjusting the optical-path L between the mirrors and the sample such that $2k_0L_2(1+\sin\theta)=2n\pi$, with $n\in\mathbb{Z}$.

To ensure the atomic transitions as illustrated in Fig. 1a and the zero detuning between different spins, it is required that the laser-frequency difference between $\{\mathbf{E}_{1x},\mathbf{E}_{1z}\}$, and that between $\{\mathbf{E}_{2x},\mathbf{E}'_{2x}\}$, exactly match the Zeeman splitting between ↑ and ↓. This can be achieved through the acousto-optical modulater (AOM), which has been widely used for two-photon Raman processes in cold atoms experiments[35,37,40–42,46]. Note that we have not shown AOM explicitly in Fig. 1.

A laser-induced loss term, characterized by γ, is generated by coupling spin-↓ atom to an excited state that is subsequently lost from the system due to spontaneous emission[47–49]. The conditional dynamics of the system under post-selection are characterized by the non-Hermitian Hamiltonian (1), after dropping the global loss term ($\sim i\gamma$).

The tight-binding model corresponding to Eq.(1) is

$$\begin{aligned}H=&-t\sum_j\left(c^\dagger_{j\uparrow}c_{j+1\uparrow}+c^\dagger_{j\downarrow}c_{j+1\downarrow}+h.c.\right)\\&+\Omega_0\sum_j\left[e^{i\phi_0}(-1)^j\left(c^\dagger_{j\uparrow}c_{j+1\downarrow}-c^\dagger_{j\uparrow}c_{j-1\downarrow}\right)+h.c.\right]\\&+\Omega_r\sum_j\left(e^{i\phi_r j}c^\dagger_{j\uparrow}c_{j\downarrow}+h.c.\right)+i\gamma\sum_j\left(c^\dagger_{j\uparrow}c_{j\uparrow}-c^\dagger_{j\downarrow}c_{j\downarrow}\right).\end{aligned} \quad (2)$$

Here the two SOCs respectively provide the nearest-neighbor and the on-site spin flip with amplitudes Ω_0 and Ω_r. We henceforth denote them as the Ω_0- and Ω_r-SOC, respectively, along with the phase parameters $\phi_0(=\phi_{1+}-\phi_{1z})$ and $\phi_r(=2\pi k_r/k_0)$. Since all the parameters in (2) are highly tunable, in this work, we fix the hopping rate t as the energy unit ($t=1$) and take $\phi_0,\phi_r\in[0,2\pi)$.

Our scheme is applicable to a wide range of alkali and alkali-earth(-like) atoms. A promising candidate is ^{173}Yb, where both

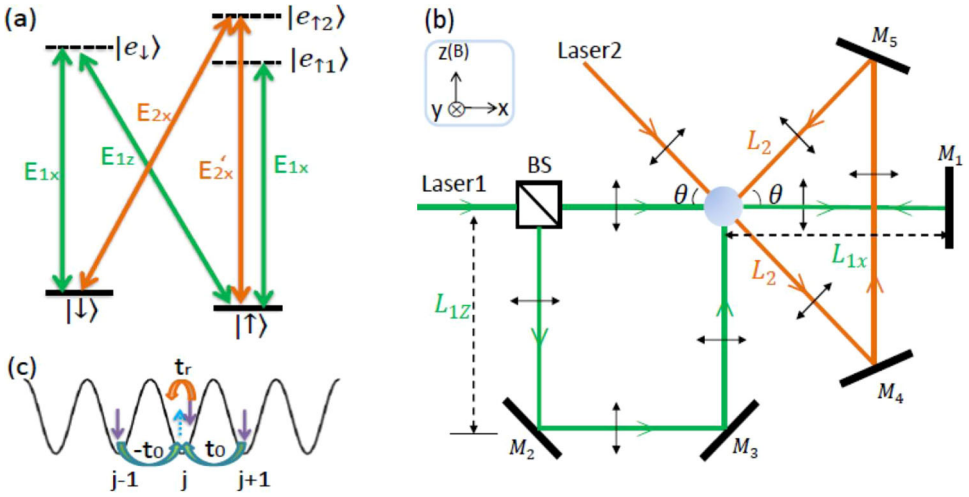

Fig. 1 Schematics of the experimental setup in generating two types of spin-orbit couplings (SOCs). a Two sets of Raman lasers couple the ground spin states via electronically excited states (dashed). **b** Laser configuration and optical-path diagram. The green and orange lines show the propagation directions of the two sets of lasers in **a**, and the black arrows indicate their polarizations. L_{1x}, L_{1z}, and L_2 are, respectively, the optical paths from the sample to mirror M_1, from the beam splitting to mirror M_2, and from the sample to M_4 (and M_5). The optical lattice potential and the Ω_0-SOC are generated by electric fields ($\mathbf{E}_{1x}$, $\mathbf{E}_{1z}$), and the Ω_r-SOC is created by electric fields ($\mathbf{E}_{2x}$, $\mathbf{E}'_{2x}$). **c** The Ω_0- and Ω_r-SOCs, respectively, generate the nearest-neighbor and the on-site spin flip with tunable strengths $\Omega_0 e^{i\phi_0}(-1)^j$ and $\Omega_r e^{i\phi_r j}$ (j is the site index).

the optical Raman lattice with band topology[46] and non-Hermitian SOC[49] have been realized using the Raman-induced ${}^1S_0 \leftrightarrow {}^3P_1$ transitions. A detailed Raman-transition scheme corresponding to Fig. 1a for ^{173}Yb can be found in [Supplementary Note 1].

NHSE and band topology. To provide insight and highlight the individual role of two SOCs, we consider the following three cases:

Case-I: $\Omega_0 = 0, \Omega_r \neq 0$

This is the lattice version of the continuum gas with non-Hermitian SOC, as implemented recently in ref. [49]. Here, following the gauge transformation $c_{j\downarrow} \to c_{j\downarrow} e^{-i\phi_r j}$, we obtain the Bloch Hamiltonian $H(k) = -2t\cos(\phi_r/2)\cos\tilde{k} + \Omega_r\sigma_x + (i\gamma - 2t\sin(\phi_r/2)\sin\tilde{k})\sigma_z$ (with $\tilde{k} = k + \phi_r/2$) and the eigen-energy

$$E_{k\pm}^{(I)} = -2t\cos(\phi_r/2)\cos\tilde{k} \pm \sqrt{\Omega_r^2 + (i\gamma - 2t\sin(\phi_r/2)\sin\tilde{k})^2}. \quad (3)$$

The eigen-spectrum supports two exceptional points at $\Omega_r = \gamma$, when $\tilde{k} = 0, \pi$ or $\phi_r = 0$.

Importantly, the system hosts NHSE for $\phi_r \neq 0, \pi$, as clearly indicated by the closed-loop topology[12,13] of (3) in the complex plane. The presence of NHSE leads to distinct spectra under PBC and OBC, and localized bulk eigen-modes near the OBC boundary (see Fig. 2a (ii), b (ii)). Nevertheless, this case is trivial in band topology, since $H(k)$ does not show any spin-winding as k traverses the Brillouin zone. As a result, the OBC spectrum does not feature any in-gap topological modes (see Fig. 2a (i), (ii)).

Case-II: $\Omega_0 \neq 0, \Omega_r = 0$

This is the case with only optical Raman lattice and dissipation. Following the transformation $c_{j\downarrow} \to (-1)^j c_{j\downarrow}$, the Bloch Hamiltonian $H(k) = 2\Omega_0\sin k(\sin\phi_0\sigma_x + \cos\phi_0\sigma_y) + (i\gamma - 2t\cos k)\sigma_z$, and the eigen-spectrum is

$$E_{k\pm}^{(II)} = \pm\sqrt{(2\Omega_0\sin k)^2 + (i\gamma - 2t\cos k)^2}. \quad (4)$$

Clearly, there is no NHSE—the spectrum (4) exhibits no loop structures in the complex plane. However, $H(k)$ possesses nontrivial band topology, as further confirmed in Fig. 2a (iii), b (iii) by the appearance of in-gap zero modes under OBC and their localized wave functions near boundaries. The topological transition occurs at $\gamma = 2\Omega_0$ for all ϕ_0, when the band gap closes at $k = \pi/2, 3\pi/2$. We note that the topological phase of a similar model under a real Zeeman field ($i\gamma \to \Gamma_z$) and $\phi_0 = 0$ has been studied in ref. [50], where the topological transition occurs at $\Gamma_z = 2t$.

One can see that the Ω_r-SOC and the Ω_0-SOC can, respectively, give rise to NHSE and band topology, as they respectively lead to spectral and wavefunction windings. In order to achieve both in a single setting, one needs to incorporate all essential gradients to satisfy both winding conditions. A natural contender is by combining both types of SOCs, as well as the on-site loss.

Case-III: $\Omega_0 \neq 0, \Omega_r \neq 0$

When both types of SOCs are switched on, an analytical form of the eigen-spectrum is generally unavailable. An exception is when $\phi_r = \pi$, under which the two SOCs are commensurate, and k is still a good quantum number. The Bloch Hamiltonian is $H(k) = (\Omega_r + 2\Omega_0\sin\phi_0\sin k)\sigma_x + 2\Omega_0\cos\phi_0\sin k\sigma_y + (i\gamma - 2t\cos k)\sigma_z$, with the eigen-spectrum

$$E_{k\pm}^{(\mathrm{III},\phi_r=\pi)} = \pm\left[\left(\Omega_r^2 + (2\Omega_0\sin k)^2 + 4\Omega_r\Omega_0\sin\phi_0\sin k + (i\gamma - 2t\cos k)^2\right]^{1/2}. \quad (5)$$

We see immediately that once $\phi_0 \neq 0, \pi$, the spectrum (5) would form a loop in the complex plane, signifying the presence of NHSE. Moreover, $H(k)$ in this case keeps a similar spin-winding pattern as in case-II, and thus the system acquires a band topology. In particular, when $\phi_0 = \pi/2, 3\pi/2$ the system has the chiral symmetry: $\sigma_y H(k)\sigma_y = -H(k)$, which protects the degenerate topological zero modes. In Fig. 3, we have numerically verified the coexistent skin and topological properties for $\phi_r = \pi$ and $\phi_0 = \pi/2$, from both the different eigen-spectra between PBC and OBC (Fig. 3a), and the localized bulk state and in-gap zero modes (Fig. 3b).

The band topology can be conveniently tuned by γ and Ω_0, Ω_r. In Fig. 4a (i), we take a specific set of Ω_0 and Ω_r, and show that by

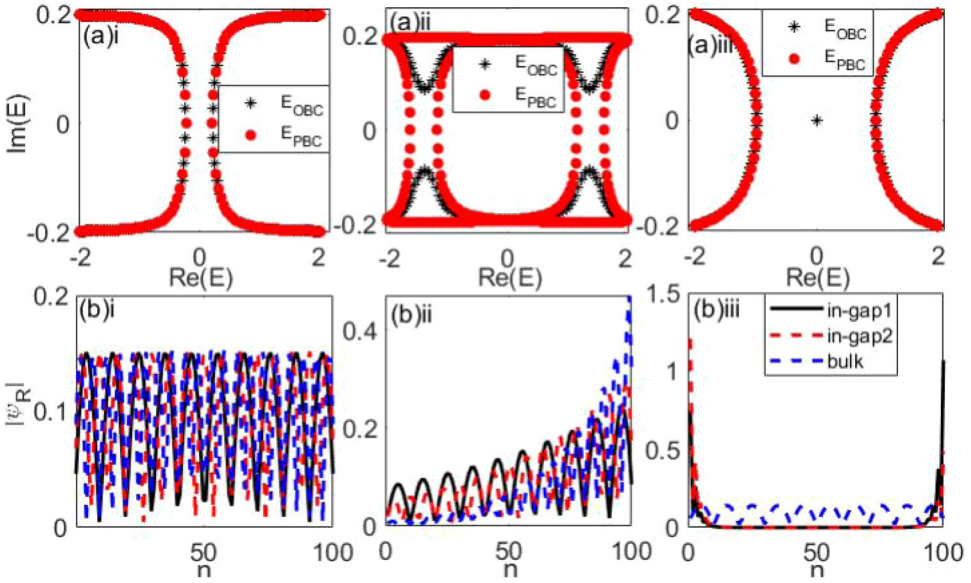

Fig. 2 Non-Hermitian skin effect and band topology for cases I and II. Eigen-spectrum (**a** (i–iii)) and spatial profile of eigen-modes (**b** (i–iii)) for case-I and -II when only one spin-orbit coupling (SOC) is present. Here we take the dissipation strength $\gamma = 0.2$, and the other parameters are $(\Omega_0, \phi_0, \Omega_r, \phi_r) = (0, -, 0.3, \pi)$ for **a** (i), **b** (i); $(0, -, 0.3, \pi/2)$ for ((a)ii,(b)ii); $(0.5, \pi/2, 0, -)$ for **a** (iii), **b** (iii). The non-Hermitian skin effect shows up only in **a** (ii), **b** (ii). **a** (iii), **b** (iii) are topological with two in-gap zero modes localized at both boundaries. Here the energy unit is taken as hopping t.

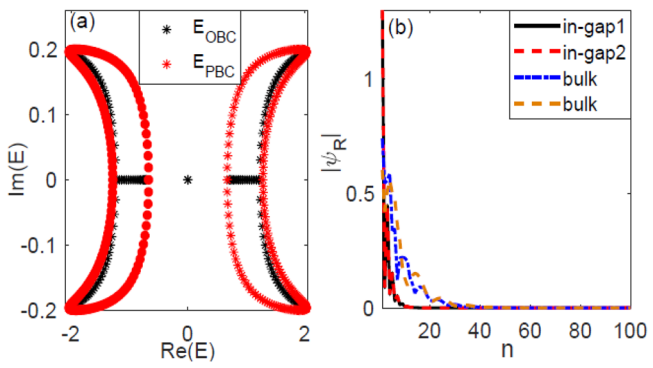

Fig. 3 Coexistence of non-Hermitian skin effect and band topology for case-III with $\phi_r = \pi, \phi_0 = \pi/2$, and $\Omega_0 = 0.5, \Omega_r = 0.3, \gamma = 0.2$. a Energy spectra under periodic boundary condition and open boundary condition in the complex plane. **b** Spatial wave functions for the two topological edge modes and two randomly chosen bulk states. Here the energy unit is taken as hopping t.

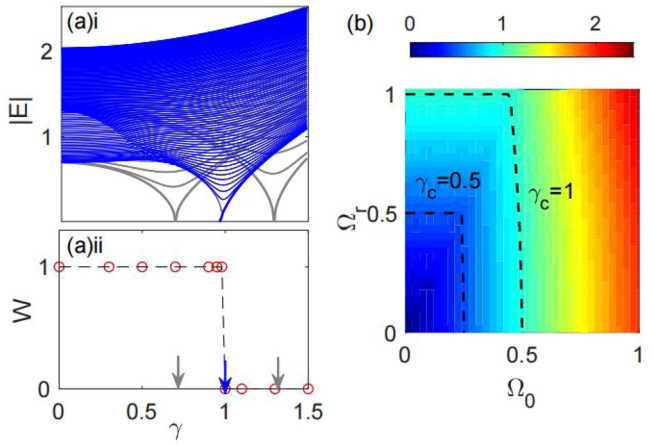

Fig. 4 Topological phase transition for case-III with $\phi_r = \pi, \phi_0 = \pi/2$. a (i, ii) The amplitude of spectrum $|E|$ under open boundary condition (blue) and the winding number W obtained from ed Brillouin zone as functions of γ. Here we take $\Omega_0 = 0.5, \Omega_r = 0.3$. The topological transition occurs at $\gamma_c \sim 1$, which differs from the periodic boundary condition predictions $\gamma_{c,PBC} = 0.7, 1.3$ (gray arrows). The periodic boundary condition eigen-spectrum is shown in gray for comparison. **b** Contour plot of γ_c in (Ω_0, Ω_r) plane (here the color bar represents the value of γ_c). The energy unit is taken as hopping t.

increasing γ to a critical γ_c, the in-gap zero modes merge into the bulk and the gap closes and reopens across this critical point. This signifies a topological transition into the trivial phase. Remarkably, γ_c is different from the gap-closing point of the eigen-spectrum (5) under PBC, where $\gamma_{c,\mathrm{PBC}} = |\Omega_r \pm 2\Omega_0|$. This is exactly the breakdown of conventional bulk-boundary correspondence under NHSE.

To restore the bulk-boundary correspondence, we adopt the non-Bloch band theory[3–6] and compute the winding number W in the GBZ. As shown in Fig. 4a (ii), W can well predict the topological transition under OBC: the in-gap zero modes emerge where $W = 1$ $(\gamma < \gamma_c)$ and vanish where $W = 0$ $(\gamma > \gamma_c)$. In fact, γ_c can be obtained analytically through the gap-closing condition of the GBZ spectrum[Methods]. The resulting topological phase diagram is given in Fig. 4b, where γ_c is plotted as functions of Ω_0 and Ω_r for the case of $\phi_0 = \pi/2$. The $\phi_0 = 3\pi/2$ case is found to share the same diagram due to symmetries[Methods].

When (ϕ_r, ϕ_0) deviate from $(\pi, \pi/2)$ and $(\pi, 3\pi/2)$, the chiral symmetry is broken, and the topological modes would split and gradually merge into the bulk. In comparison, NHSE is much more robust, which can persist for all (ϕ_r, ϕ_0) except for $\phi_r = 0$ and two discrete points (π, π) and $(\pi, 0)$[Supplementary Note 2]. In Table 1, we summarize the conditions for band topology and NHSE for cases I–III. The main message is that both SOCs are indispensable in achieving NHSE and topology simultaneously. Their combination shows an intriguing interplay effect, instead of being a trivial superposition. For instance, the application of Ω_r-SOC in case-III changes the topology condition as compared to case-II, and the Ω_0- SOC changes the skin condition as compared

Table 1 Conditions for achieving topological phase and non-Hermitian skin effect (NHSE) for various cases.

		Topological	NHSE	Topological + NHSE
Case-I	$\Omega_0 = 0,\ \Omega_r \neq 0$	×	$\phi_r \neq 0, \pi$	×
Case-II	$\Omega_0 \neq 0,\ \Omega_r = 0$	$\gamma < 2\Omega_0$	×	×
Case-III	$\Omega_0 \neq 0,\ \Omega_r \neq 0$	$\phi_r = \pi, \phi_0 = \frac{\pi}{2}, \frac{3\pi}{2}$ and $\gamma < \gamma_c$	$\phi_r \neq 0$ and $(\phi_r, \phi_0) \neq (\pi, 0), (\pi, \pi)$	$\phi_r = \pi, \phi_0 = \frac{\pi}{2}, \frac{3\pi}{2}$ and $\gamma < \gamma_c$

Ω_0 and Ω_r are, respectively, the nearest-neighbor and the on-site spin-flip amplitudes, γ is the dissipation strength, and ϕ_r, ϕ_0 are the phase parameters. " × " means absence for all occasions.

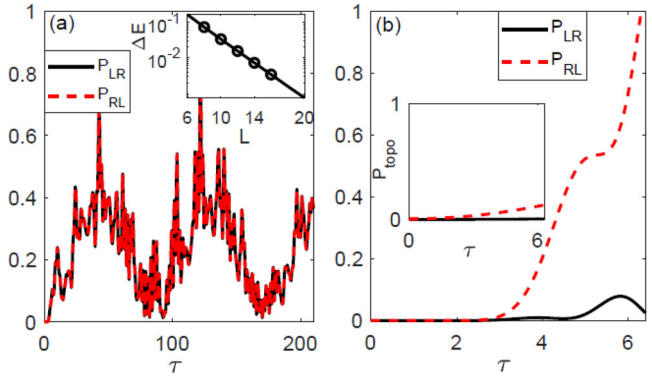

Fig. 5 Topological transport with and without non-Hermitian skin effect. Edge-to-edge transport properties for the topological system without (**a**) and with (**b**) non-Hermitian skin effect. We take $\Omega_0 = 0.5, \Omega_r = 0.3$, and $\gamma = 0$ (**a**), 0.2 (**b**). In the main plots, the system size $L = 8$. The inset of **b** shows the contribution from the topological edge states. Here the energy unit is hopping t, and the time unit is $\hbar/t$.

to case-I. In particular, for the latter case, the presence of Ω_0-SOC further broadens the parameter region of observing skin modes, signifying a positive effect of band topology in enhancing NHSE.

Dynamic detection. To detect the topological phase with NHSE, we propose an edge-to-edge transport measurement. In the Hermitian case, the topological edge modes play the dominant role in such transport [51]. However, in the presence of NHSE, the transport is expected to be significantly modified since all bulk modes also localize near the edge. To examine such an effect, we compare two topological systems in our setup, one is Hermitian at $\gamma = 0$, and the other is with NHSE at finite γ. We study the probability of particle occupation at the β-edge of the system at time τ, when the initial state starts from the α-edge ($\alpha, \beta =$ L or R)

$$P_{\alpha\beta}(\tau) = \left|\langle\beta|e^{-iH\tau}|\alpha\rangle\right|^2. \tag{6}$$

To eliminate the difference caused by spin, we take the initial state as the equal population of ↑ and ↓ and show its dynamics in Fig. 5. In the Hermitian case (Fig. 5a), the left-to-right (P_{LR}) and right-to-left (P_{RL}) transports are identical. As a manifestation of the topological edge states, the oscillation frequency of P_{LR} (or P_{RL}), as given by the energy gap between the two edge modes in a finite-size system, is found to decay exponentially with increasing system size (inset of Fig. 5a). In the presence of NHSE (Fig. 5b), the transport properties are dramatically different. Due to the localization of skin modes at the left boundary, the transport shows a strong directional preference towards the left side, namely. In this case, the topological edge modes play little role in affecting the dynamics (inset of Fig. 5b). These features distinguish the topological phases with and without NHSE.

Optical lattices with sharp boundaries can be implemented using box-trap potentials[52–56], where the spatial extent of an edge is determined by the optical wavelength ~1 μm (much smaller than the typical trap length ~10–100 μm). Such a small imperfection does not visibly change the dynamics in Fig. 5 [Supplementary Note 3]. Even sharper edges (~10 nm) can be created via the dark state in atomic Λ-system[57–59]. Alternatively, without edges, the NHSE can also manifest itself in bulk dynamics[16,21,22]. Indeed we have confirmed that NHSE can lead to visible directional bulk transport under typical harmonic trapping potentials[Supplementary Note 3].

For the detection of the non-Bloch band topology, one may further resort to quench dynamics or measurement of the biorthogonal chiral displacement[60,61]. Alternatively, topological edge states may be probed through a time-integrated state tomography[28].

Discussion

We have proposed a realistic scheme for utilizing the SOCs and the spin-dependent dissipation in ultracold atoms to engineer NHSE with band topology. We emphasize that both SOCs are indispensable in the scheme. Their mutual interference, along with their interplay with the on-site dissipation, determines the ultimate parameter regime for skin modes with nontrivial band topology (Table 1).

For future studies, an intriguing possibility would be tuning ϕ_r away from π such that the two SOCs become incommensurate. The competition between quasiperiodicity and NHSE would potentially lead to unique localization features[26,27]. Further generalization of our scheme to higher dimensions would offer the opportunity for achieving Weyl exceptional rings[62], high-order skin effect, and band topology featuring corner or hinge modes[63–65]. Moreover, the implementation of NHSE in ultracold atoms paves the way for exploring collective phenomena therein due to interatomic interactions, which are easily tunable through Feshbach resonances. Our proposal, therefore, ushers in a wide variety of possibilities for the quantum simulation of non-Hermitian physics.

Methods

Derivation of the tight-binding model. To derive the tight-binding model, we expand the field operator $\psi_\sigma(x) = \sum_i \omega_{n=0}(x - x_i)c_{i\sigma}$, where $\omega_{n=0}(x)$ is the lowest-band Wannier function, and i is the index of lattice sites. In this way, the second-quantized single-particle Hamiltonian can be reduced to the tight-banding model, with the following parameters:

(1) the nearest-neighbor hopping term

$$t = -\int dx\omega_0(x)\left(\frac{p_x^2}{2m} - V_0\cos(2k_0x)\right)\omega_0(x-a). \tag{7}$$

(2) the on-site spin-flip terms

$$t^j_{\uparrow\downarrow} = \int dx\omega_0^*(x - x_j)M_r e^{i2k_rx}\omega_0(x - x_j) \equiv e^{i\phi_r j}\Omega_r, \tag{8}$$

$$t^j_{\downarrow\uparrow} = \int dx\omega_0^*(x - x_j)M_r e^{-i2k_rx}\omega_0(x - x_j) \equiv e^{-i\phi_r j}\Omega_r, \tag{9}$$

where the amplitude $\Omega_r = M_r\int dx\omega_0^2(x)e^{i2k_rx}$, and the corresponding phase $\phi_r = 2k_ra = 2\pi k_r/k_0$. Note that here we pin down the coordinate of the j-site atom as $x_j = ja$, with $a = \pi/k_0$ as the lattice spacing.

(3) the nearest-neighbor spin-flip terms

$$\begin{aligned} t^{j,j+1}_{\uparrow\downarrow} &= \int dx\omega_0^*(x - x_j)(M_0\sin k_0xe^{i\phi_0})\omega_0(x - x_{j+1}) \\ &\equiv e^{i\phi_0}(-1)^j\Omega_0, \end{aligned} \tag{10}$$

$$\begin{aligned} t^{j,j-1}_{\uparrow\downarrow} &= \int dx\omega_0^*(x - x_j)(M_0\sin k_0xe^{i\phi_0})\omega_0(x - x_{j-1}) \\ &\equiv -e^{i\phi_0}(-1)^j\Omega_0, \end{aligned} \tag{11}$$

where the amplitude $\Omega_0 = M_0 \int dx\omega_0(x)\sin k_0 x\omega_0(x-a)$. Again we have used $x_j = ja$.

Finally we get the tight-binding model as Eq. (2) in the main text.

Non-Bloch band theory. We have adopted the non-Bloch band theory[3–6] to investigate the topological properties for case-III with non-Hermitian skin effect. Replacing the vector k by $\beta = e^{ik}$ in the Bloch Hamiltonian, the non-Bloch Hamiltonian in the spin space can be written as

$$H(\beta) = \begin{pmatrix} i\gamma - t(\beta+\beta^{-1}) & \Omega - e^{i\phi_0}t_{so}(\beta-\beta^{-1}) \\ \Omega + e^{-i\phi_0}t_{so}(\beta-\beta^{-1}) & -i\gamma + t(\beta+\beta^{-1}) \end{pmatrix}. \quad (12)$$

Then the eigenvalues E follow

$$E^2 = \left[i\gamma - t(\beta+\beta^{-1})\right]^2 + [\Omega - e^{i\phi_0}t_{so}(\beta-\beta^{-1})] \\ (\Omega + e^{-i\phi_0}t_{so}(\beta-\beta^{-1})). \quad (13)$$

For a given value of E, the four solutions of β can be organized as $|\beta_1| \le |\beta_2| \le |\beta_3| \le |\beta_4|$. Imposing the condition $|\beta_2| = |\beta_3|$ would pin down all β-solutions for the generalized Brillouin zone (GBZ).

The non-Bloch winding number accumulated in the GBZ is then

$$W = \frac{i}{2\pi}\int_\beta \sum_{\nu=\pm} \langle u_{\nu L}(\beta)|\partial_\beta|u_{\nu R}(\beta)\rangle, \quad (14)$$

where the right and left eigenvectors are defined through $H(\beta)|u_{\nu R}\rangle = E_{\beta\nu}|u_{\nu R}\rangle$ and $H^\dagger(\beta)|u_{\nu L}\rangle = E^*_{\beta\nu}|u_{\nu L}\rangle$. Note that $H(\beta)$ satisfies the chiral symmetry $\sigma_y H(\beta)\sigma_y = -H(\beta)$, for $\phi_0 = \pi/2, 3\pi/2$.

Topological phase transition point. The gap-closing condition, indicative of the topological transition, requires the solution $E = 0$ of (13), i.e.,

$$0 = [i\gamma_c - t(\beta+\beta^{-1})]^2 + [\Omega - e^{i\phi_0}t_{so}(\beta-\beta^{-1})] \\ [\Omega + e^{-i\phi_0}t_{so}(\beta-\beta^{-1})]. \quad (15)$$

In combination with the continuum band requirement: $|\beta_1| \le |\beta_2| = |\beta_3| \le |\beta_4|$, we obtain the relation between γ_c and Ω_0, Ω_r. In particular, since the topological zero modes are protected by the chiral symmetry when $\phi_0 = \pi/2, 3\pi/2$, in the following, we shall discuss the topological transition in these two cases separately.

1. $\phi_0 = \pi/2$

The solution of γ_c as a function of Ω_0, Ω_r can be divided into two regimes

$$(1) \quad \text{for } \Omega_0 \le \Omega_{0c} : \gamma_c = \Omega_r; \quad (16)$$

$$(2) \quad \text{for } \Omega_0 \ge \Omega_{0c} : 2(t\gamma_c + \Omega_r\Omega_0) = (t+\Omega_0) \\ \sqrt{(\Omega_r+\gamma_c)^2 + 4t^2 - 4\Omega_0^2} - (t-\Omega_0)\sqrt{(\Omega_r-\gamma_c)^2 + 4t^2 - 4\Omega_0^2}. \quad (17)$$

Here Ω_{0c} satisfies

$$(t+\Omega_{0c})\left(\sqrt{\Omega_r^2 + t^2 - \Omega_{0c}^2} - \Omega_r\right) = (t-\Omega_{0c})\sqrt{t^2 - \Omega_{0c}^2}. \quad (18)$$

2. $\phi_0 = 3\pi/2$

From Eq. (13), we see that the case with $\phi_0 = 3\pi/2$ can be related to that with $\phi_0 = \pi/2$ by the transformation $\beta \to \beta^{-1}$. This means that we can directly utilize the four β-solutions in $\phi_0 = \pi/2$ case, i.e., $|\beta_1| \le |\beta_2| = |\beta_3| \le |\beta_4|$, to obtain the solutions in the $\phi_0 = 3\pi/2$ case as $|\beta_4|^{-1} \le |\beta_3|^{-1} = |\beta_2|^{-1} \le |\beta_1|^{-1}$, without any change of the spectrum E. Therefore the topological transition points in the two cases should be identical. We have numerically confirmed that γ_c has the same dependence on the parameters Ω_0, Ω_r as in the case of $\phi_0 = \pi/2$.

Data availability

The data that support the results of this study are available from the corresponding author upon reasonable request.

Received: 21 March 2022; Accepted: 16 September 2022;
Published online: 13 October 2022

References

1. El-Ganainy, R. et al. Non-Hermitian physics and PT symmetry. *Nat. Phys.* **14**, 11 (2018).
2. Ashida, Y., Gong, Z. & Ueda, M. Non-Hermitian physics. *Adv. Phys.* **69**, 3 (2020).
3. Yao, S. & Wang, Z. Edge states and topological invariants of non-Hermitian systems. *Phys. Rev. Lett.* **121**, 086803 (2018).
4. Yao, S., Song, F. & Wang, Z. Non-Hermitian chern bands. *Phys. Rev. Lett.* **121**, 136802 (2018).
5. Yang, Z., Zhang, K., Fang, C. & Hu, J. Non-Hermitian bulk-boundary correspondence and auxiliary generalized brillouin zone theory. *Phys. Rev. Lett.* **125**, 226402 (2020).
6. Yokomizo, K. & Murakami, S. Non-Bloch band theory of non-Hermitian systems. *Phys. Rev. Lett.* **123**, 066404 (2019).
7. Martinez Alvarez, V. M., Barrios Vargas, J. E. & Foa Torres, L. E. F. Non-Hermitian robust edge states in one dimension: anomalous localization and eigenspace condensation at exceptional points. *Phys. Rev. B* **97**, 121401(R) (2018).
8. Lee, C. H. & Thomale, R. Anatomy of skin modes and topology in non-Hermitian systems. *Phys. Rev. B* **99**, 201103(R) (2019).
9. Song, F., Yao, S. & Wang, Z. Non-Hermitian skin effect and chiral damping in open quantum systems. *Phys. Rev. Lett.* **123**, 170401 (2019).
10. Deng, T.-S. & Yi, W. Non-Bloch topological invariants in a non-Hermitian domain-wall system. *Phys. Rev. B* **100**, 035102 (2019).
11. Borgnia, D. S., Kruchkov, A. J. & Slager, R.-J. Non-Hermitian boundary modes and topology. *Phys. Rev. Lett.* **124**, 056802 (2020).
12. Zhang, K., Yang, Z. & Fang, C. Correspondence between winding numbers and skin modes in non- Hermitian systems. *Phys. Rev. Lett.* **125**, 126402 (2020).
13. Okuma, N., Kawabata, K., Shiozaki, K. & Sato, M. Topological origin of non-Hermitian skin effects. *Phys. Rev. Lett.* **124**, 086801 (2020).
14. Yi, Y. & Yang, Z. Non-Hermitian skin modesinduced by on-site dissipations and chiral tunneling effect. *Phys. Rev. Lett.* **125**, 186802 (2020).
15. Li, L., Lee, C. H. & Gong, J. Topological switch for non-Hermitian skin effect in cold-atom systems with loss. *Phys. Rev. Lett.* **124**, 250402 (2020).
16. Longhi, S. Probing non-Hermitian skin effect and non-Bloch phase transitions. *Phys. Rev. Res.* **1**, 023013 (2019).
17. Longhi, S. Non-Bloch-band collapse and chiral zener tunneling. *Phys. Rev. Lett.* **124**, 066602 (2020).
18. Guo, C.-X., Liu, C.-H., Zhao, X.-M., Liu, Y. & Chen, S. Exact solution of non-Hermitian systems with generalized boundary conditions: size-dependent boundary effect and fragility of the skin effect. *Phys. Rev. Lett.* **127**, 116801 (2021).
19. Vecsei, P. M., Denner, M. M., Neupert, T. & Schindler, F. Symmetry indicators for inversion-symmetric non-Hermitian topological band structures. *Phys. Rev. B* **103**, L201114 (2021).
20. Schindler, F. & Prem, A. Dislocation non-Hermitian skin effect. *Phys. Rev. B* **104**, L161106 (2021).
21. Mao, L., Deng, T. & Zhang, P. Boundary condition independence of non-Hermitian Hamiltonian dynamics. *Phys. Rev. B* **104**, 125435 (2021).
22. Liu, C.-H. & Chen, S. Information restraint in open quantum systems. *Phys. Rev. B* **104**, 174305 (2021).
23. Liu, C.-H., Zhang, K., Yang, Z. & Chen, S. Helical damping and dynamical critical skin effect in open quantum systems. *Phys. Rev. Res.* **2**, 043167 (2020).
24. Longhi, S. Non-Bloch PT symmetry breaking in non-Hermitian photonic quantum walks. *Opt. Lett.* **44**, 5804 (2019).
25. Xiao, L. et al. Observation of Non-Bloch PT symmetry and exceptional points. *Phys. Rev. Lett.* **126**, 230402 (2021).
26. Longhi, S. Topological phase transition in non-Hermitian quasicrystals. *Phys. Rev. Lett.* **122**, 237601 (2019).
27. Liu, Y., Wang, Y., Liu, X.-J., Zhou, Q. & Chen, S. Exact mobility edges, PT-symmetry breaking and skin effect in one-dimensional non-Hermitian, quasicrystals. *Phys. Rev. B* **103**, 014203 (2021).
28. Xiao, L. et al. Non-Hermitian bulk-boundary correspondence in quantum dynamics. *Nat. Phys.* **16**, 761 (2020).
29. Weidemann, S. et al. Topological funneling of light. *Science* **368**, 311 (2020).
30. Wang, K. et al. Generating arbitrary topological windings of a non-Hermitian band. *Science* **371**, 1240 (2021).
31. Helbig, T. et al. Generalized bulk-boundary correspondence in non-Hermitian topolectrical circuits. *Nat. Phys.* **16**, 747 (2020).
32. Ghatak, A., Brandenbourger, M., van Wezel, J. & Coulais, C. Observation of non-hermitian topology and its bulk-edge correspondence in an active mechanical metamaterial. *Proc. Natl Acad. Sci. USA* **117**, 29561 (2020).
33. Hatano, N. & Nelson, D. R. Localization transition in non-Hermitian quantum mechanics. *Phys. Rev. Lett.* **77**, 570 (1996).
34. Lee, T. E. Anomalous edge state in a non-Hermitian lattice. *Phys. Rev. Lett.* **116**, 133903 (2016).
35. Lin, Y.-J., Jiménez-García, K. & Spielman, I. B. Spin orbit-coupled Bose Einstein condensates. *Nature* **471**, 83 (2011).
36. Zhang, J.-Y. et al. Collective dipole oscillations of a spin-orbit coupled bose-einstein condensate. *Phys. Rev. Lett.* **109**, 115301 (2012).
37. Wang, P. et al. Spin-orbit coupled degenerate fermi gases. *Phys. Rev. Lett.* **109**, 095301 (2012).
38. Cheuk, L. W. et al. Spin-injection spectroscopy of a spin-orbit coupled fermi gas. *Phys. Rev. Lett.* **109**, 095302 (2012).

39. Qu, C., Hamner, C., Gong, M., Zhang, C. & Engels, P. Observation of Zitterbewegung in a spin-orbit-coupled Bose-Einstein condensate. *Phys. Rev. A* **88**, 021604(R) (2013).
40. Huang, L. et al. Experimental realization of two-dimensional synthetic spin-orbit coupling in ultracold Fermi gases. *Nat. Phys.* **12**, 540 (2016).
41. Meng, Z. et al. Experimental observation of a topological band gap opening in ultracold fermi gases with two-dimensional spin-orbit coupling. *Phys. Rev. Lett.* **117**, 235304 (2016).
42. Wu, Z. et al. Realization of two-dimensional spin-orbit coupling for Bose-Einstein condensates. *Science* **354**, 83 (2016).
43. Sun, W. et al. Highly controllable and robust 2D spin-orbit coupling for quantum gases. *Phys. Rev. Lett.* **121**, 150401 (2018).
44. Mancini, M. et al. Observation of chiral edge states with neutral fermions in synthetic Hall ribbons. *Science* **349**, 1510 (2015).
45. Stuhl, B. K., Lu, H.-I., Aycock, L. M., Genkina, D. & Spielman, I. B. Visualizing edge states with an atomic Bose gas in the quantum Hall regime. *Science* **349**, 1514 (2015).
46. Song, B. et al. Observation of symmetry-protected topological band with ultracold fermions. *Sci. Adv.* **4**, eaao4748 (2018).
47. Li, J. et al. Observation of parity-time symmetry breaking transitions in a dissipative Floquet system of ultracold atoms. *Nat. Commun.* **10**, 855 (2019).
48. Lapp, S., Ang'ong'a, J., Alex An, F. & Gadway, B. Engineering tunable local loss in a synthetic lattice of momentum states. *N. J. Phys.* **21**, 045006 (2019).
49. Ren, Z. et al. Topological control of quantum states in non-Hermitian spin-orbit-coupled fermions. *Nat. Phys.* https://doi.org/10.1038/s41567-021-01491-x (2022).
50. Liu, X.-J., Liu, Z.-X. & Cheng, M. Manipulating topological edge spins in one-dimensional optical lattice. *Phys. Rev. Lett.* **110**, 076401 (2013).
51. de Léséleuc, S. et al. Observation of symmetry-protected topological phase of interacting bosons with Rydberg atoms. *Science* **365**, 775 (2019).
52. Gaunt, A. L., Schmidutz, T. F., Gotlibovych, I., Smith, R. P. & Hadzibabic, Z. Bose Einstein condensation of atoms in a uniform potential. *Phys. Rev. Lett.* **110**, 200406 (2013).
53. Chomaz, L. et al. Emergence of coherence via transverse condensation in a uniform quasi-two-dimensional Bose gas. *Nat. Commun.* **6**, 6162 (2015).
54. Mukherjee, B. et al. Homogeneous atomic Fermi gases. *Phys. Rev. Lett.* **118**, 123401 (2017).
55. Hueck, K. et al. Two-dimensional homogeneous Fermi gases. *Phys. Rev. Lett.* **120**, 060402 (2018).
56. Tajik, M. et al. Designing arbitrary one-dimensional potentials on an atom chip. *Opt. Express* **27**, 33474 (2019).
57. Lacki, M., Baranov, M. A., Pichler, H. & Zoller, P. Nanoscale "Dark State" optical potentials for cold atoms. *Phys. Rev. Lett.* **117**, 233001 (2016).
58. Jendrzejewski, F. et al. Subwavelength-width optical tunnel junctions for ultracold atoms. *Phys. Rev. A* **94**, 063422 (2016).
59. Wang, Y. et al. Dark state optical lattice with a subwavelength spatial structure. *Phys. Rev. Lett.* **120**, 083601 (2018).
60. Li, T., Sun, J.-Z., Zhang, Y.-S. & Yi, W. Non-Bloch quench dynamics. *Phys. Rev. Res.* **3**, 023022 (2021).
61. Wang, K. et al. Detecting non-Bloch topological invariants in quantum dynamics. *arXiv*. https://arxiv.org/abs/2107.14741 (2021).
62. Xu, Y., Wang, S.-T. & Duan, L.-M. Weyl exceptional rings in a three-dimensional dissipative cold atomic gas. *Phys. Rev. Lett.* **118**, 045701 (2017).
63. Kawabata, K., Sato, M. & Shiozaki, K. Higher-order non-Hermitian skin effects. *Phys. Rev. B* **102**, 205118 (2020).
64. Li, L., Lee, C. H., Mu, S. & Gong, J. Critical non-Hermitian skin effect. *Nat. Commun.* **11**, 5491 (2020).
65. Benalcazar, W. A., Bernveig, B. A. & Hughes, T. L. Quantized electric multipole insulators. *Science* **357**, 61 (2017).

Acknowledgements

The work is supported by the National Key Research and Development Program of China (2018YFA0307600 and 2017YFA0304100), the National Natural Science Foundation of China (No.12074419, 12134015, and 11974331), and the Strategic Priority Research Program of Chinese Academy of Sciences (No. XDB33000000).

Author contributions

The project was initiated by X.C. and supervised by X.C. and W.Y. L.Z. performed the numerical calculations and L.H. provided assistance on double checking the data. All authors contributed to analyzing the results and writing the manuscript.

Competing interests

The authors declare no competing interests.

Additional information

Supplementary information The online version contains supplementary material available at https://doi.org/10.1038/s42005-022-01021-y.

Correspondence and requests for materials should be addressed to Wei Yi or Xiaoling Cui.

Peer review information *Communications Physics* thanks the anonymous reviewers for their contribution to the peer review of this work. Peer reviewer reports are available.

Reprints and permission information is available at http://www.nature.com/reprints

Publisher's note Springer Nature remains neutral with regard to jurisdictional claims in published maps and institutional affiliations.